



Temperature versus type: Which is the determining factor in biomass-based electrocatalyst performance?

Wendu Zhang^a, Shilin Wei^a, Peiyao Bai^a, Weiqi Liu^a, Chuangchuang Yang^a, Lang Xu^{a,*}

^a MOE Key Laboratory of Coal Processing and Efficient Utilization, School of Chemical Engineering and Technology, China University of Mining and Technology, 1 Daxue Road, Xuzhou, Jiangsu 221116, China

ARTICLE INFO

Keywords:

Processing temperature
Part
Consistency
Convergence
Divergence

ABSTRACT

Having high natural abundance enables biomass to be deliberately employed to prepare electrocatalysts by annealing processing. The great diversity of biomass originating from different types or parts is leading to concerns about consistency of product performance. Taking acidic and alkaline electroreduction of dioxygen as the object of study, we have demonstrated that processing temperatures exert much more powerful influence over structures and activities of biomass-based electrocatalysts than which parts of biomass are used. It has been found that initial discrepancies due to different parts are narrowed and aggregated by arithmetic means in terms of structures and activities at the same elevated temperatures, whereas there are wide gaps between electrocatalysts prepared at different processing temperatures even though they stem from the same part of biomass. We have also explored systematically how processing temperatures tailor pore width distributions and nitrogen species distributions and how these parameters tune mass transport and reaction intermediate absorption strengths with concomitant performance on the basis of a great deal of experimental and theoretical evidence. Hence, this work helps to address growing concerns about consistency of biomass-based electrocatalysts and to indicate the feasibility of their large-scale manufactures because temperature is the determining factor, not type.

1. Introduction

Compared to noncarbon materials, carbon is readily used as an electrocatalyst support because of its high electronic conductivity [1–5]. To achieve high electrochemical performance, it is essential to acquire good carbon sources, and how to define ‘good’ varies considerably [6–12]. Viewed from the renewable and diversified standpoint, biomass indeed represents a suitable selection of carbon sources, which can be processed into a vast array of high-performance electrocatalysts by means of thermal treatments [13–20].

Nevertheless, employing biomass to produce electrocatalysts is often accompanied by one question: could biomass from different types or parts be converted into consistent catalysts in terms of structures and activities under the same processing method? The answer is of great practical importance – after all, it is extremely hard to keep every batch of feedstock identical in large-scale industrial processes, no matter what source is taken. It has recently been reported that origins, organs, and species of biomass have considerable impact on electrochemical behaviors of biomass-based carbons [21,22]. Concerns are therefore being raised as to whether even subtle deviations from raw materials can bring

about nonnegligible differences in product performance.

Let us temporarily shift the focus from biomass itself to processing methods. Conversions of biomass into catalysts inevitably require high-temperature treatments in which a series of significant physicochemical changes such as carbonization, pore formation, and surface functionalization takes place [23–30]. Thus, the *processing temperature* is an important parameter for affecting biomass-based catalyst performance. In this sense, though there might be fundamental distinction between untreated biomass of different *types* or *parts* in terms of intrinsic structures and compositions owing to their diverse biological functions, could such differences diminish or instead become more pronounced after thermal treatments? And could catalytically active sites dissipate and eventually disappear at elevated temperatures, degrading catalytic performance? Endeavors to address these questions allow us to raise the possibilities that we gain consistent and predictable performance of catalysts made from varied types or parts of biomass simply by controlling processing temperatures.

In this work five different parts of hibiscus, a worldwide flowering plant, are selected as sources. Structures of two series of biomass-based electrocatalysts prepared from these parts or at different processing

* Corresponding author.

E-mail address: lang.xu@cumt.edu.cn (L. Xu).

<https://doi.org/10.1016/j.apcatb.2023.122391>

Received 27 October 2022; Received in revised form 29 December 2022; Accepted 7 January 2023

Available online 9 January 2023

0926-3373/© 2023 Elsevier B.V. All rights reserved.

temperatures are determined in detail and their electrocatalytic activities are further compared in terms of oxygen reduction reaction (ORR) under alkaline and acidic conditions. Our results show that the differences in structures and activities of biomass-based electrocatalysts induced by dissimilar parts of biomass are far smaller than those engendered by different temperatures. The processing temperatures are able to change the electrocatalytic performance by tailoring pore width distributions and nitrogen species distributions, which involve mass transport and reaction intermediate absorption strengths respectively. In addition to different parts being capable of causing *convergent* structures at high temperatures, this study also discloses the tendency to average out the variations in structures and activities if diverse parts of biomass are mixed in the first place, which means that it is not necessary to subdivide biomass into parts but to treat it as a whole. This is because processing temperature is now proved to be the most important factor in determining biomass-based electrocatalyst performance.

2. Experimental section

2.1. Preparations of two series of biomass-based electrocatalysts

Carbon sources selected in this work come from floral organs and stems of hibiscus (*Hibiscus rosa-sinensis*), which were collected, cleansed, and dried in the China's tropical island – Hainan. Specifically, they are segregated into five parts: (i) stamens and carpels (SC), (ii) petals (P), (iii) sepals and receptacles (SR), (iv) epidermis and cortex (EC), and (v) xylem and pith (XP). Among them, (i) – (iii) belong to floral organs of hibiscus: (i) is fertile while (ii) and (iii) are sterile; moreover, (iv) and (v) are the outer and inner layers of hibiscus stems, respectively. The photographs of these five parts are shown in Fig. 1. Each part of hibiscus in the raw state was converted to the corresponding biochar by heating it at 400 °C for two hours in a tube furnace along with a sustained N₂ flow. Then, two series of hibiscus-based electrocatalysts were prepared using different parts and dissimilar processing temperatures:

Series A: same temperature, different parts. In this series, each part of hibiscus in the biochar form (0.5 g) was ball-milled with melamine (2.0 g), KHCO₃ (2.0 g), and KOH (0.5 g), dispensing with any solvent, followed by annealing under flowing N₂ first at 300 °C for two hours and then at 900 °C for another two hours. The product obtained was successively rinsed with HCl (1 M) and water, and finally dried. The nomenclature for this series of hibiscus-based electrocatalysts is H-900-x, in which 'H' is short for hibiscus, '900' refers to the final annealing temperature, and 'x' denotes one part of hibiscus, namely the five parts SC, P, SR, EC, and XP corresponding to the five products H-900-SC, H-900-P, H-900-SR, H-900-EC, and H-900-XP, respectively. Furthermore, the two parts of hibiscus, EC and XP, were mixed and used as the starting material, the product being thereby denoted H-900-EC+XP.

Series B: same part, different temperatures. One part of hibiscus – EC was employed as the carbon source for this series of electrocatalysts. The preparation method for Series B is the same as for Series A described above, except that the final annealing temperature in this series varies from 700 °C to 1000 °C. The nomenclature used in Series B is H-t-EC, where 'H', 't', and 'EC' represent hibiscus, the final annealing temperature applied, and the part of hibiscus – epidermis and cortex, respectively. As a result, the Series B electrocatalysts include H-700-EC, H-800-EC, H-900-EC, and H-1000-EC.

2.2. Structural characterization and performance measurements

Structures and electrocatalytic performance of the two series of hibiscus-based electrocatalysts were evaluated with a set of characterization methods and electrochemical techniques, which have been outlined in detail in the [Supplementary Material](#). Additionally, the theoretical calculations were carried out using the VASP software [31–34], and the details of the calculations can also be found in the [Supplementary Material](#).

3. Results and discussion

3.1. Morphological variation arising from different parts

The first column of Fig. 1 shows the photographs of the five parts of raw hibiscus, which belong to floral organs (SC, P, and SR) and stems (EC and XP). These five parts have the distinctive appearances and of course their different biological functions. Under the same processing conditions, the five parts can be transformed into the five electrocatalysts, that is, H-900-SC, H-900-P, H-900-SR, H-900-EC, and H-900-XP, their scanning electron microscopy (SEM) images being presented in the second (lower magnification) and the third columns of Fig. 1. It is obvious that the five products prepared at the same temperature exhibit the widely different morphologies: some have relatively smooth surfaces (e.g. H-900-XP) whereas others possess rather rugged ones that may be more conducive to the improvement in electrocatalytic performance (e.g. H-900-EC). In view of the same preparation method applied, the discrepancies in the micrometer-sized morphologies should be ascribed to the different parts of hibiscus.

To further investigate the coarse electrocatalysts, the nanoscale morphologies of H-900-EC have been identified using a transmission electron microscope (TEM). Fig. 2a and b show that H-900-EC contains the gauze-like structure with the wrinkled and rough surfaces. According to the high-resolution TEM images (Fig. 2c and d), H-900-EC, with numerous nanopores being seen across the entire electrocatalyst, is overwhelmingly in an amorphous form, which is further confirmed by the selected area electron diffraction pattern shown in the inset to Fig. 2b, although there are a few discontinuous lattice fringes resulting from some degree of graphitization of carbon at the elevated temperature. Furthermore, the energy-dispersive spectrum (EDS) mapping of H-900-EC measured using a TEM, as exhibited in Fig. 2e–h, clearly shows that nitrogen is evenly distributed over the carbon-based electrocatalyst, an indication that the preparation method described in this work allows for the well-spread introduction of dopants into the carbon structure. This is not easy to achieve, in particular considering the uneven surface of H-900-EC where additives tend to accumulate around certain regions.

3.2. Effects of parts and processing temperatures on pore width distributions

Pores concerned in electrocatalysis usually comprise micropores, mesopores, and macropores, mainly associated with mass transport. Micropores and mesopores, known as *nanopores*, are often estimated using physisorption isotherm measurements, while macropores can be investigated by the mercury intrusion porosimetry (MIP) method [35, 36]. To understand the influences of different parts and different processing temperatures over pore width distributions, the Series A (same temperature, different parts) and Series B (same part, different temperatures) electrocatalysts have been prepared and compared. It is noteworthy that H-900-EC+XP (belonging to Series A) has also been made by mixing the two parts EC and XP together prior to the thermal processing, the purpose of which is to determine whether structures and activities of products prepared by mixtures of different parts tend to be averages of those by each component of the mixtures.

3.2.1. Nanopores

The first and second columns of Fig. 3 show that the N₂ (77 K) adsorption-desorption isotherms and the nanopore width distributions using the quenched solid density functional theory (QSDFT) model for the two series of hibiscus-based electrocatalysts, respectively. In terms of the curve shapes, the differences among the Series A electrocatalysts are markedly smaller than those among the Series B ones, indicating that the processing temperature has a much greater impact on the nanopore width distributions than the part. It is also notable that the isotherm of H-900-EC+XP lies between those of H-900-EC and H-900-XP (Fig. 3a), suggesting the tendency to average out the part-dependent variability.

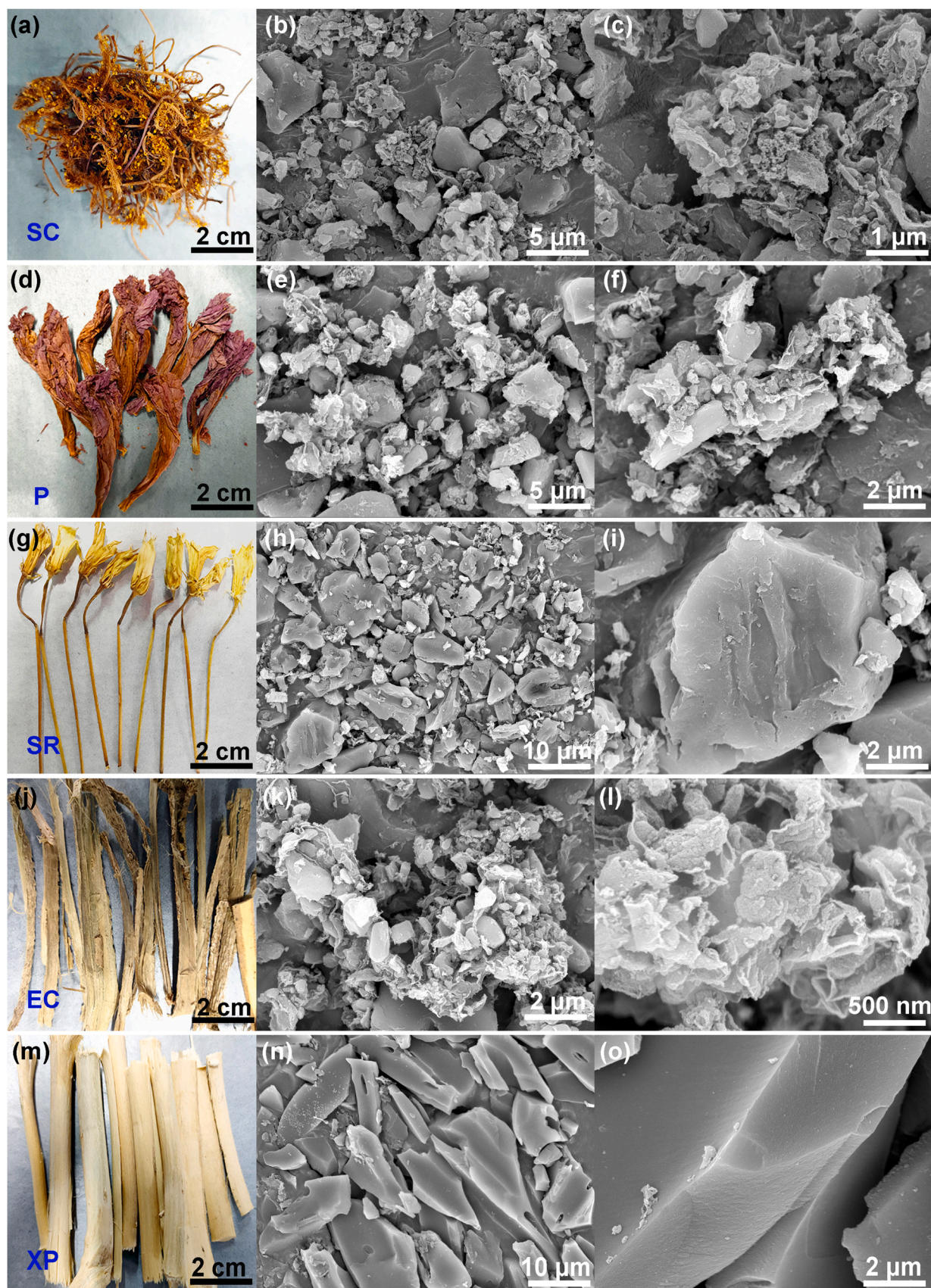


Fig. 1. Photographic images of SC (a), P (d), SR (g), EC (j), and XP (m). SEM images of H-900-SC (b,c), H-900-P (e,f), H-900-SR (h,i), H-900-EC (k,l), and H-900-XP (n,o).

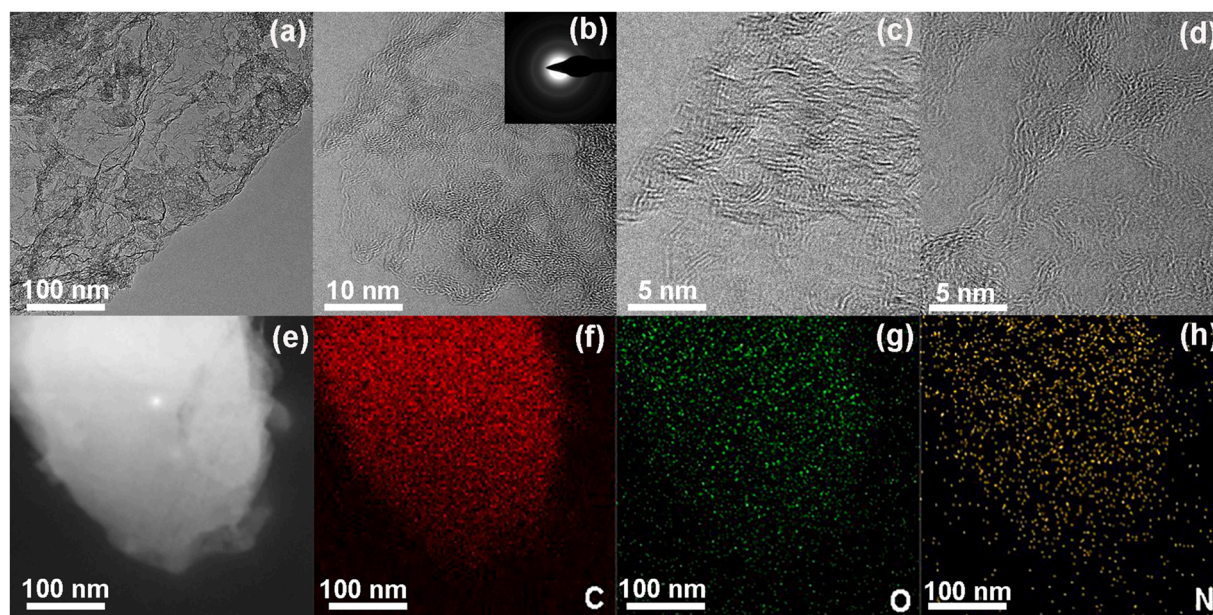


Fig. 2. TEM images (a-d) and EDS mapping images (e-h) of H-900-EC. The selected area electron diffraction pattern is shown in the inset to (b).

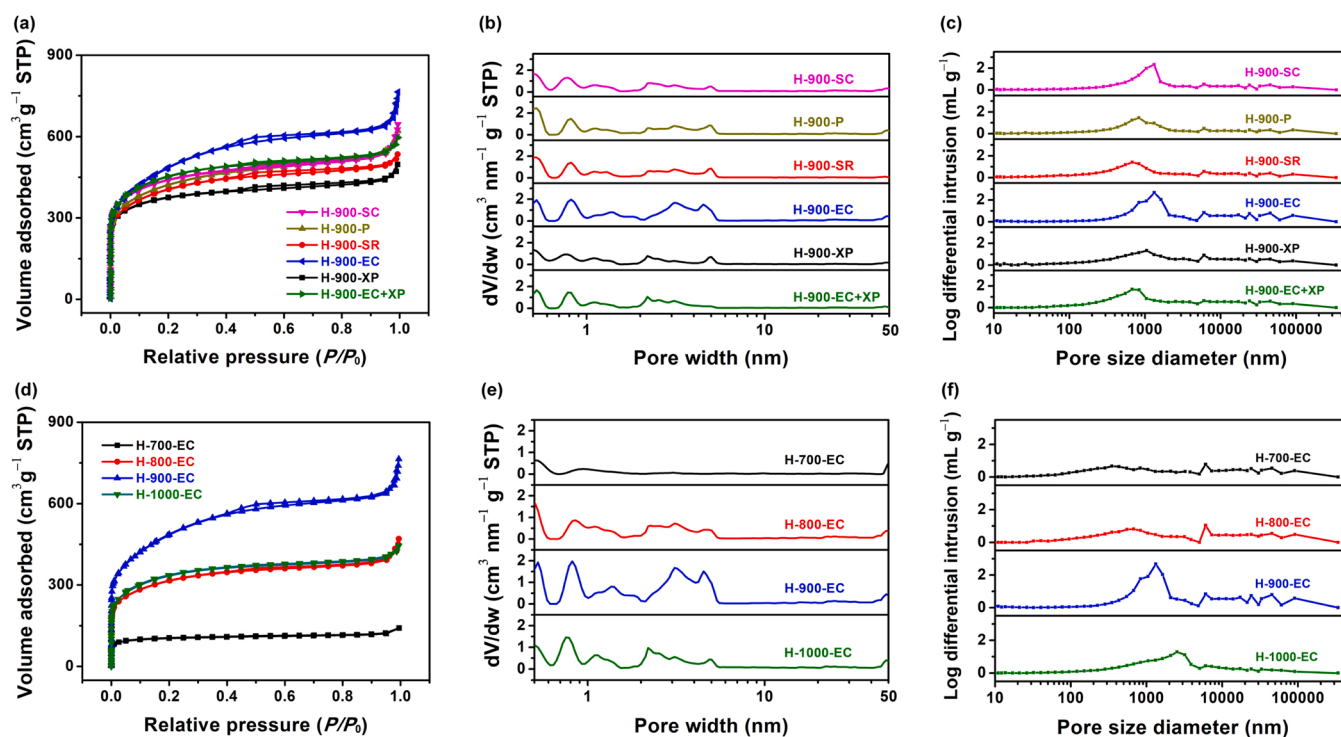


Fig. 3. Nitrogen adsorption-desorption isotherms of Series A (a) and Series B (d). Nanopore width distributions of Series A (b) and Series B (e) according to the QSDFT model. Macropore width distributions of Series A (c) and Series B (f) using the mercury intrusion method.

Furthermore, the nanopore and surface data of the two series of electrocatalysts have been determined by using the QSDFT analysis. As summarized in Table 1, the surface areas of Series A and B fall in the range $1355.6 \text{ m}^2 \text{ g}^{-1}$ – $1620.1 \text{ m}^2 \text{ g}^{-1}$ and $468.6 \text{ m}^2 \text{ g}^{-1}$ – $1620.1 \text{ m}^2 \text{ g}^{-1}$, respectively, and the pore volumes of Series A and B lie in the range $0.65 \text{ cm}^3 \text{ g}^{-1}$ – $0.92 \text{ cm}^3 \text{ g}^{-1}$ and $0.18 \text{ cm}^3 \text{ g}^{-1}$ – $0.92 \text{ cm}^3 \text{ g}^{-1}$, respectively. Obviously, the Series A electrocatalysts prepared from the different parts at the same processing temperature possess the more centralized distributions of nanopore widths than their Series B counterparts made from the same part at the different temperatures. Apart

from the overall nanopores, micropores or mesopores alone are in accord with this trend, that is, Series A having the narrow ranges of textural properties of either micropores or mesopores and the opposite of Series B. It is interesting to note that the pore volumes and surface areas of H-900-EC+XP approximate to the averages (i.e. arithmetic means) of the corresponding values of H-900-EC and H-900-XP, regardless of whether they are whole nanopores or individual micropores or mesopores, with the advantage that the predictability of products can be achieved if different parts of biomass are mixed together. (It should be stressed that no need for classification according

Table 1

Tabulated data for surfaces and pores of Series A and B obtained from the QSDFT (for nanopores) and the MIP (for macropores) analyses.

| Electrocatalyst | S_{QSDFT} ($\text{m}^2 \text{g}^{-1}$) | $S_{0-2 \text{ nm}}$ ($\text{m}^2 \text{g}^{-1}$) | $S_{2-50 \text{ nm}}$ ($\text{m}^2 \text{g}^{-1}$) | V_{QSDFT} ($\text{cm}^3 \text{g}^{-1}$) | $V_{0-2 \text{ nm}}$ ($\text{cm}^3 \text{g}^{-1}$) | $V_{2-50 \text{ nm}}$ ($\text{cm}^3 \text{g}^{-1}$) | Porosity | Tortuosity |
|-----------------|---|---|--|--|--|---|----------|------------|
| H-900-SC | 1445.4 | 1051.9 | 393.5 | 0.76 | 0.41 | 0.35 | 0.66 | 2.5 |
| H-900-P | 1418.6 | 1045.8 | 372.8 | 0.72 | 0.40 | 0.32 | 0.63 | 2.6 |
| H-900-SR | 1376.3 | 1021.7 | 354.6 | 0.68 | 0.37 | 0.31 | 0.62 | 2.8 |
| H-900-EC | 1620.1 | 1123.7 | 496.4 | 0.92 | 0.49 | 0.43 | 0.67 | 2.4 |
| H-900-XP | 1355.6 | 1014.6 | 341.0 | 0.65 | 0.35 | 0.30 | 0.62 | 2.5 |
| H-900-EC+XP | 1511.8 | 1119.2 | 392.6 | 0.79 | 0.42 | 0.37 | 0.64 | 2.5 |
| H-700-EC | 468.6 | 441.5 | 27.1 | 0.18 | 0.14 | 0.04 | 0.48 | 3.7 |
| H-800-EC | 1162.7 | 885.3 | 277.4 | 0.51 | 0.29 | 0.22 | 0.56 | 3.3 |
| H-1000-EC | 1202.0 | 944.2 | 257.8 | 0.58 | 0.33 | 0.25 | 0.54 | 3.1 |

to parts is cost-effective from an industrial perspective.).

Based on the physisorption data mentioned above, it is reasonable to conclude that the nanopore width distributions of hibiscus-based electrocatalysts are influenced much more by the processing temperature than the part. As shown in Table 1, both pore volumes and surface areas first increase as the temperature rises from 700 °C to 900 °C but finally decrease if it is raised further to 1000 °C (see Series B), which can be ascribed to the shrinkage of nanopore structure at the excessively high temperature [37]. On the other hand, the nanopore width distributions of the Series A electrocatalysts, all of which are prepared at the same processing temperature, bear close resemblance to each other even though they derive from the completely different parts that possess the dissimilar morphologies (Fig. 1) with diverse functions. In other words, differences in properties of initial states diminish at very elevated temperatures, resulting in *convergence* (i.e. similar structures). Moreover, the tendency to average out the variations of pore structures allows such differences further to decrease.

3.2.2. Macropores

The macropore width distributions of Series A and B using the MIP technique are exhibited in Fig. 3c and f, respectively. Like the physisorption measurements with N_2 , the mercury intrusion data provide comparable information on the different ways in which the macropore widths of the two series of hibiscus-based electrocatalysts are distributed, that is, broadly similar distributions for Series A and dissimilar distributions for Series B, showing the processing temperature still has a much stronger influence on macropores than the part. From the MIP measurements, the two important parameters – porosity and tortuosity can be obtained, which reflect the structural properties of pores in terms of mass transport, as summarized in Table 1. For the same-part, different-temperature Series B electrocatalysts, the porosity increases from 0.48 to 0.67 whereas the tortuosity decreases from 3.7 to 2.4 as the temperature is raised from 700 °C to 900 °C. Because a higher porosity and a lower tortuosity help to reduce resistance of mass transport [38, 39], elevating the processing temperature is capable of improving mass transport. However, the overheating leads to the unwanted change: that

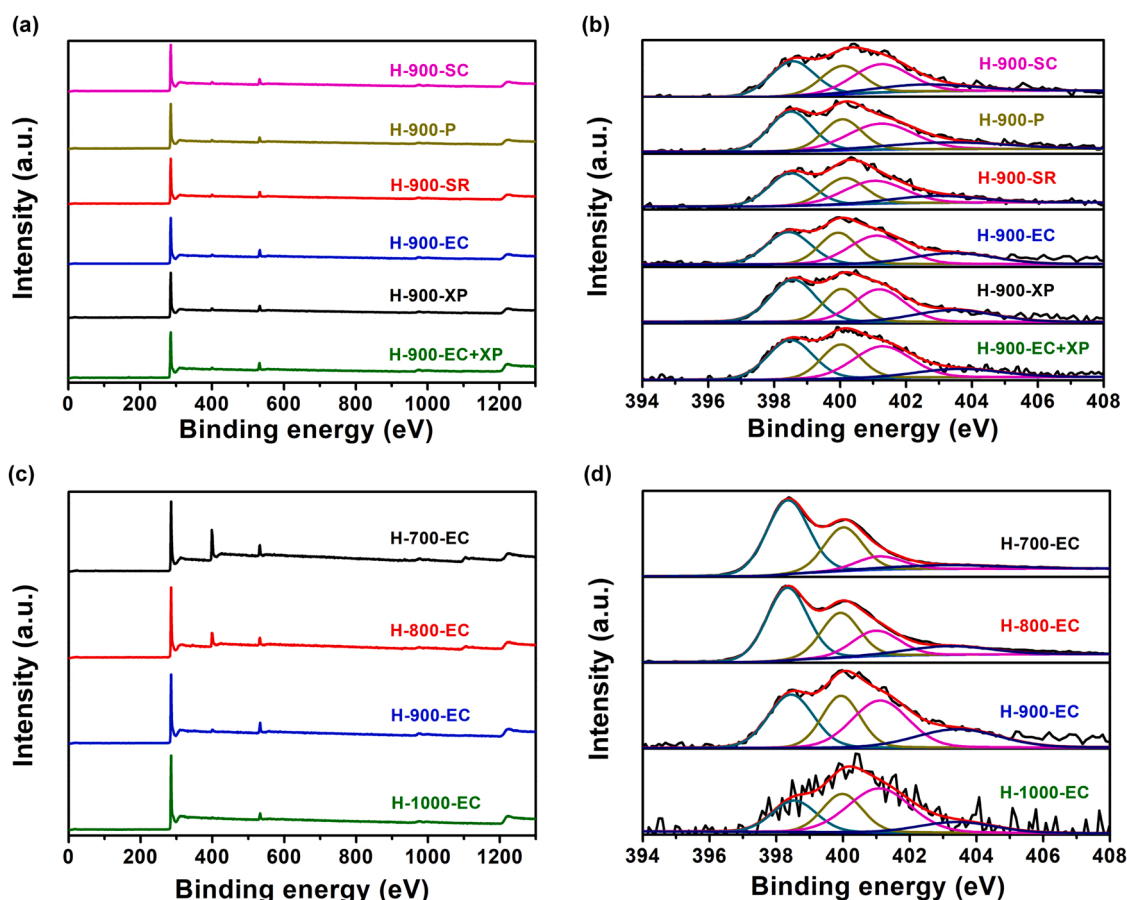


Fig. 4. Survey XPS spectra of Series A (a) and Series B (c). Raw data, deconvoluted peaks and fit for N 1s high-resolution XPS spectra of Series A (b) and Series B (d).

is, the porosity begins to decline while the tortuosity rises at 1000 °C. By contrast, the same-temperature, different-part Series A electrocatalysts share the close porosity (0.62–0.67) and tortuosity (2.4–2.8), taking on the convergent character. Furthermore, the porosity and tortuosity of H-900-EC+XP are transitional between the respective values of H-900-EC and H-900-XP, indicative of the ability to average out macropores. Consequently, the processing temperature exerts a far larger influence on the macropore width distributions and their attendant parameters in comparison with the part, a situation akin to that experienced by nanopores.

3.3. Effects of parts and processing temperatures on elemental distributions

Surface elemental analyses of the two series of hibiscus-based electrocatalysts are conducted using the X-ray photoelectron spectroscopy (XPS) technique. Fig. 4 exhibits the survey and N 1 s high-resolution XPS spectra of Series A and B. In general, every survey spectrum contains C 1 s, N 1 s, and O 1 s peaks, centered at around 284.5 eV, 401.5 eV, and 532.5 eV, respectively (Fig. 4a and c), while the N 1 s high-resolution spectra can each be deconvoluted into four peaks that are assigned to oxidized (403.2 eV), graphitic (401.2 eV), pyrrolic (400.1 eV), and pyridinic (398.4 eV) nitrogens (Fig. 4b and d) [40–42]. More specifically, according to the survey XPS spectra of the Series A electrocatalysts (Fig. 4a), the elements of the same type have the approximately equal peak intensities, inferring that the identical elements (C, N, or O) are quite close to each other in contents for this series of electrocatalysts obtained from the diverse parts at the same processing temperature. Likewise, the shapes and intensities of the N 1 s high-resolution XPS spectra along with their deconvoluted peaks among the Series A electrocatalysts are all similar (Fig. 4b), implying the similar nitrogen species distributions for this series. In contrast, there are apparent discrepancies in the XPS spectra of Series B originating from the same part at the different processing temperatures. As shown in Fig. 4c, the hibiscus-based electrocatalysts prepared at the relatively lower temperatures (H-700-EC and H-800-EC) have the remarkably higher peaks of nitrogen than their higher-temperature counterparts (H-900-EC and H-1000-EC), illustrating that volatile N atoms evaporate gradually and are carried away by a flowing atmosphere as the temperature is raised. In addition, the N 1 s high-resolution spectra of the Series B electrocatalysts (Fig. 4d) manifest the very large difference in the nitrogen species distributions at various temperatures. Phenomenologically, it can therefore be generalized that it is the processing temperature that has the far greater effect on elemental distributions than the part.

Table 2 lists the information on the surface elements and nitrogen species distributions present in Series A and B, obtained from the XPS analyses. The C, N, and O contents of the same-temperature Series A electrocatalysts range from 89.6 at% to 90.7 at%, 3.4–4.2 at%, and 5.6–6.7 at%, respectively, showing that their elemental distributions are highly centralized. Moreover, the relative contents and ratios of the four nitrogens are very close, confirming that the nitrogen species distributions of Series A bear striking resemblance to each other. By comparison,

the N content of Series B drops sharply from 23.8 at% to 1.3 at% as the processing temperature is raised from 700 °C to 1000 °C. From the perspective of variations in relative contents, it is worthwhile to note that as the processing temperature is steadily increasing, the pyridinic nitrogen undergoes the successive loss from 53.4% to 21.3% while the graphitic nitrogen follows the opposite trend: increasing from 11.6% to 42.6%. Furthermore, the ratios of pyridinic to graphitic nitrogens are given in Table 2. For Series A, the average ratios are 1.0, which means that pyridinic and graphitic nitrogens are of equal amounts among the electrocatalysts obtained from the dissimilar parts using the same processing temperature. In comparison, such ratios change from 4.6 of H-700-EC (pyridinic nitrogen being in the vast majority) to 0.5 of H-1000-EC (graphitic nitrogen becoming twice as numerous). As will be described below, the pyridinic/graphitic ratio that can be adjusted by the processing temperature has a significant influence on absorption strengths of reaction intermediates and hence the electrocatalytic performance.

In short, it can be concluded from the XPS measurements that the processing temperature rather than the part greatly alters the elemental distributions of biomass-based electrocatalysts. Element contents and nitrogen species distributions can be tailored by regulating the processing temperature, resulting in consistent and predictable products even if different parts are employed (see Series A), in much the same way as pore width distributions.

3.4. Important factors influencing electrocatalytic performance

Different extents of influences from processing temperatures and parts on structures lead inevitably to variations in electrocatalyst performance. A suite of electrochemical techniques has been employed to explore alkaline and acidic electrocatalysis of ORR by means of the two series of hibiscus-based electrocatalysts.

3.4.1. Cyclic voltammetry (CV) and linear sweep voltammetry (LSV)

The electrocatalytic performance in the alkaline medium is first investigated. As displayed in Fig. 5a and c, the cathodic peaks that occur as dioxygen is reduced in the O₂-saturated aqueous KOH solution disappear in N₂, showing that both Series A and B have the capabilities to act as ORR electrocatalysts. Typically, the more positive the reduction peak potentials, the stronger the catalytic power of ORR electrocatalysts. From Fig. 5a, it is clear that there is little difference in the peak potentials for the Series A electrocatalysts, among which H-900-EC has the most positive peak potential while the peak potential of H-900-EC+XP is situated between that of H-900-EC and H-900-XP. This indicates that the hibiscus-based electrocatalysts processed at the same temperature from the different parts provide the similar performance despite H-900-EC having the optimal activity and the catalytic properties of H-900-EC+XP being intermediate between those of H-900-EC and H-900-XP. By contrast, the peak potentials of the Series B electrocatalysts are markedly dissimilar, together with the fact that H-900-EC has the even more positive peak potential than commercial Pt/C, suggesting that there are significant differences in catalytic performance for the hibiscus-based

Table 2

Atomic percentages of surface elements (C, N, and O) and relative amounts of nitrogen species for Series A and B from the XPS measurements.

| Electrocatalyst | C (at%) | N (at%) | O (at%) | Pyridinic (%) | Pyrrolic (%) | Graphitic (%) | Oxidized (%) | Pyridinic Graphitic |
|-----------------|---------|---------|---------|---------------|--------------|---------------|--------------|---------------------|
| H-900-SC | 90.4 | 3.6 | 6.0 | 29.6 | 24.3 | 32.8 | 13.3 | 0.9 |
| H-900-P | 90.4 | 4.0 | 5.6 | 32.1 | 21.3 | 32.3 | 14.3 | 1.0 |
| H-900-SR | 90.7 | 3.4 | 5.9 | 31.6 | 24.3 | 30.7 | 13.4 | 1.0 |
| H-900-EC | 89.6 | 3.7 | 6.7 | 31.2 | 23.1 | 32.1 | 13.6 | 1.0 |
| H-900-XP | 89.9 | 4.2 | 5.9 | 33.5 | 21.0 | 28.9 | 16.6 | 1.1 |
| H-900-EC+XP | 90.1 | 3.8 | 6.1 | 31.6 | 23.5 | 32.3 | 12.6 | 1.0 |
| H-700-EC | 70.8 | 23.8 | 5.4 | 53.4 | 27.8 | 11.6 | 7.2 | 4.6 |
| H-800-EC | 80.1 | 15.0 | 4.9 | 42.8 | 20.7 | 25.3 | 11.2 | 1.7 |
| H-1000-EC | 93.9 | 1.3 | 4.8 | 21.3 | 23.6 | 42.6 | 12.5 | 0.5 |

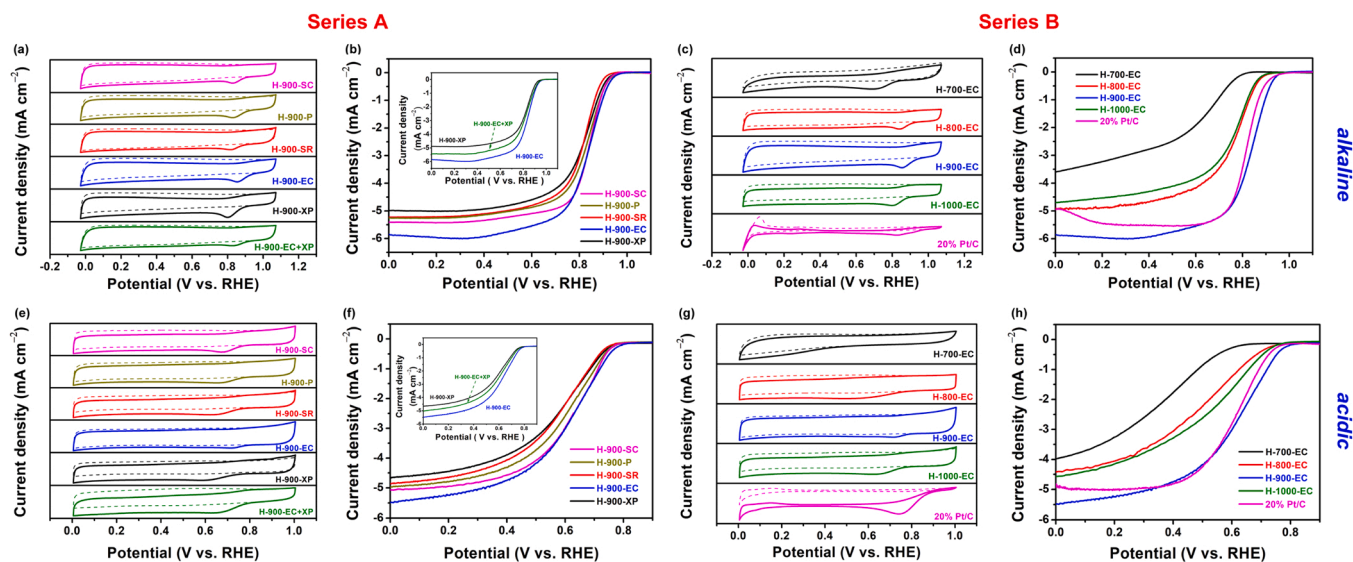


Fig. 5. CV and LSV curves of Series A in the alkaline (a,b) and acidic (e,f) electrolytes. CV and LSV curves of Series B in the alkaline (c,d) and acidic (g,h) electrolytes. Solid and dotted lines correspond to electrochemical experiments conducted in the O₂- and N₂-saturated electrolytes, respectively. The insets to (b) and (f) show the comparisons of LSV curves for H-900-EC, H-900-XP, and H-900-EC+XP in the respective electrolytes.

electrocatalysts prepared at the different processing temperatures in spite of the same part used, as shown in Fig. 5c. This comparison can thus be rationalized on the basis that the catalytic behaviors of biomass-based electrocatalysts are affected much more by the processing temperature than by the part, which is consistent with the structural trends as described above.

More detailed comparisons of catalytic performance between the two series of hibiscus-based electrocatalysts are made by means of LSV curves, from which three parameters can be read, that is, limiting current density (j_{lim}), half-wave potential ($E_{1/2}$), and onset potential (E_{on}). The ORR performance usually becomes enhanced when E_{on} and $E_{1/2}$ shift to more positive values and j_{lim} rises. The three parameter values of the Series A and B electrocatalysts, which are extracted from their corresponding LSV curves (Fig. 5b and d), are summarized in Table 3. It can be seen that the same-temperature Series A electrocatalysts possess the similar values for the three parameters, particularly for E_{on} and $E_{1/2}$ with their respective differences being fairly small (≤ 0.03 V). As expected, the three parameter values of H-900-EC+XP are the arithmetic means of their corresponding numbers of H-900-EC and H-900-XP, signifying that fluctuations in electrocatalytic activities due to structures that vary according to parts average out. On the other hand, there are marked differences in the ORR parameters, as for the different-temperature Series B electrocatalysts, among which H-900-EC offers the best performance, even superior to Pt/C. As a generalization, the impact that the processing temperature has on the structures and the concomitant activities

(in the alkaline electrolyte) of biomass-based electrocatalysts is much greater than for the part.

Next, the electrocatalytic ORR properties of both Series A and B are probed in the acidic medium. Fig. 5e-h show the CV and LSV curves of all the hibiscus-based electrocatalysts alongside Pt/C in the N₂- and/or O₂-saturated aqueous H₂SO₄ solutions, their corresponding electrochemical parameter values being also summarized in Table 3. Clearly, the trend in improving the electrocatalytic performance in the acidic electrolyte is the same as in the alkaline one mentioned above: the variety of ORR behaviors resulting from the same-part, different-temperature electrocatalysts (Series B) is much more diverse than for the same-temperature, different-part ones (Series A), which substantiates that the processing temperature remains overwhelmingly the most important factor in influencing the electrocatalytic performance regardless of pH.

3.4.2. Tafel plots, rotating ring-disk electrode (RRDE), and chronoamperometry

With regard to the optimum electrocatalyst H-900-EC, its kinetics, selectivity, and stability are further compared with its Pt/C counterparts in the alkaline and acidic media. It is known that the Tafel equation gives information concerning electrochemical kinetics in terms of the Tafel slope [43,44]. As can be seen from the Tafel plots of H-900-EC and Pt/C in aqueous KOH (Fig. 6a) and aqueous H₂SO₄ (Fig. 6e), H-900-EC has the lower Tafel slope than Pt/C in either electrolyte, indicative of the faster kinetics for the alkaline and acidic ORR processes by means of the

Table 3

Key electrochemical parameters for Series A and B, alongside Pt/C, in the alkaline and acidic electrolytes.^a

| Electrocatalyst | Alkaline (0.1 M KOH) | | | | | Acidic (0.5 M H ₂ SO ₄) | | | | |
|-----------------|----------------------|-----------|-----------|----------|------|--|-----------|-----------|----------|------|
| | E_{on} | $E_{1/2}$ | j_{lim} | R_{ct} | W | E_{on} | $E_{1/2}$ | j_{lim} | R_{ct} | W |
| H-900-SC | 0.97 | 0.84 | 5.41 | 52.8 | 0.08 | 0.82 | 0.62 | 5.07 | 4.1 | 0.05 |
| H-900-P | 0.97 | 0.83 | 5.26 | 50.5 | 0.08 | 0.81 | 0.60 | 4.97 | 3.9 | 0.05 |
| H-900-SR | 0.95 | 0.81 | 5.23 | 53.2 | 0.09 | 0.79 | 0.59 | 4.82 | 3.9 | 0.06 |
| H-900-EC | 0.98 | 0.84 | 5.95 | 51.3 | 0.08 | 0.83 | 0.62 | 5.45 | 3.9 | 0.05 |
| H-900-XP | 0.95 | 0.81 | 4.95 | 52.4 | 0.09 | 0.80 | 0.59 | 4.61 | 4.0 | 0.06 |
| H-900-EC+XP | 0.97 | 0.82 | 5.45 | 51.7 | 0.08 | 0.81 | 0.61 | 4.98 | 3.9 | 0.05 |
| H-700-EC | 0.81 | 0.61 | 3.50 | 75.8 | 0.18 | 0.66 | 0.39 | 3.80 | 5.9 | 0.11 |
| H-800-EC | 0.92 | 0.77 | 4.92 | 62.3 | 0.11 | 0.76 | 0.50 | 4.35 | 4.6 | 0.08 |
| H-1000-EC | 0.91 | 0.75 | 4.69 | 42.6 | 0.10 | 0.78 | 0.54 | 4.49 | 3.0 | 0.07 |
| Pt/C | 0.95 | 0.82 | 5.40 | — | — | 0.81 | 0.61 | 4.95 | — | — |

^a Units of symbols: E_{on} and $E_{1/2}$: V vs. RHE; j_{lim} : mA cm⁻²; R_{ct} and W : Ω.

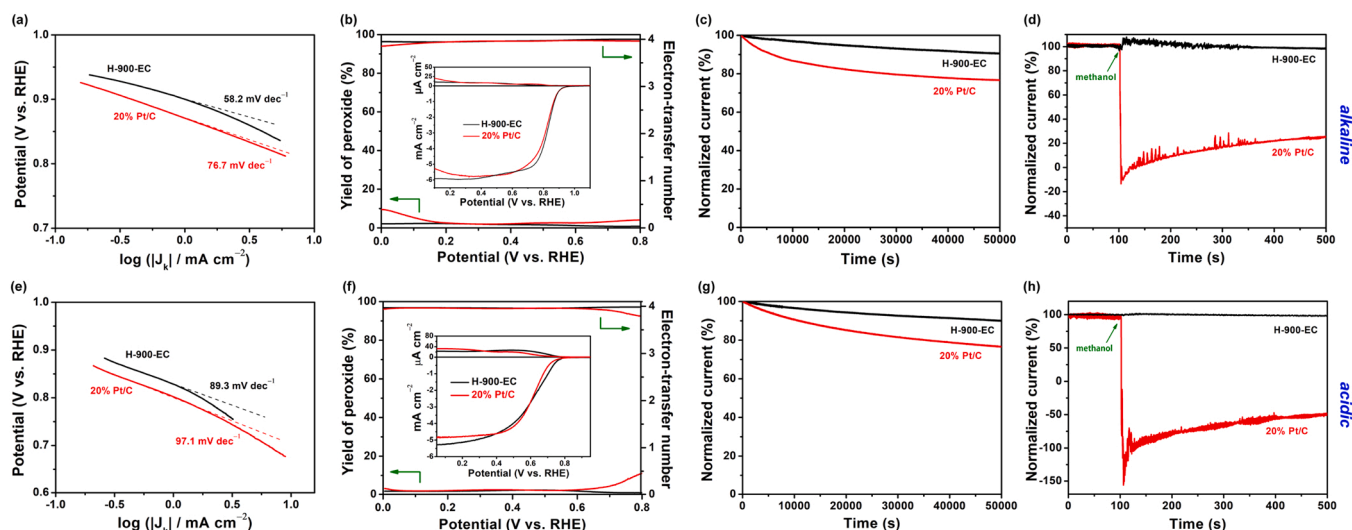


Fig. 6. Tafel plots (a,e), RRDE measurements (b,f), catalytic current stability (c,g), and methanol tolerance tests (d,h) of H-900-EC and Pt/C in the alkaline (upper diagram) and acidic (lower diagram) electrolytes. Note the ring and disk voltammograms for the RRDE shown in the insets to (b) and (f).

former. Furthermore, the electrocatalytic selectivity has been studied using the RRDE technique by which 2- or 4-electron reduction of dioxygen can be determined [45,46]. As shown in Fig. 6b, the electron-transfer number and the percentage yield of peroxide (the 2-electron by-product) of H-900-EC are 3.97% and 1.65%, respectively, H-900-EC exhibiting the 4-electron process with an even higher selectivity than Pt/C in the alkaline solution. Likewise, the electron-transfer number (3.97) and the percentage yield of peroxide (1.67%) of H-900-EC are improved compared with those of Pt/C in the acidic electrolyte, as displayed in Fig. 6f, demonstrating the optimal selectivity for H-900-EC irrespective of pH conditions. Additionally, alkaline and acidic stabilities can be compared between H-900-EC and Pt/C by employing the chronoamperometric method. Under the same electrochemical conditions, Pt/C suffers a more rapid decay of currents than

H-900-EC (Fig. 6c and g), together with little resistance to methanol exposure for the former (Fig. 6d and h). As a consequence, H-900-EC is capable of surpassing the commercial Pt/C in terms of catalytic kinetics, selectivity, and stability, which can be attributed to its unique pore width distribution and nitrogen species distribution, as discussed in the following section.

3.5. Structure-activity relationships

Compared to parts, processing temperatures have a much stronger influence on performance through changing pore width distributions and nitrogen species distributions of biomass-based electrocatalysts. It is important to understand how these two aspects affect electrocatalytic activities. First, the electrochemical impedance spectroscopy (EIS)

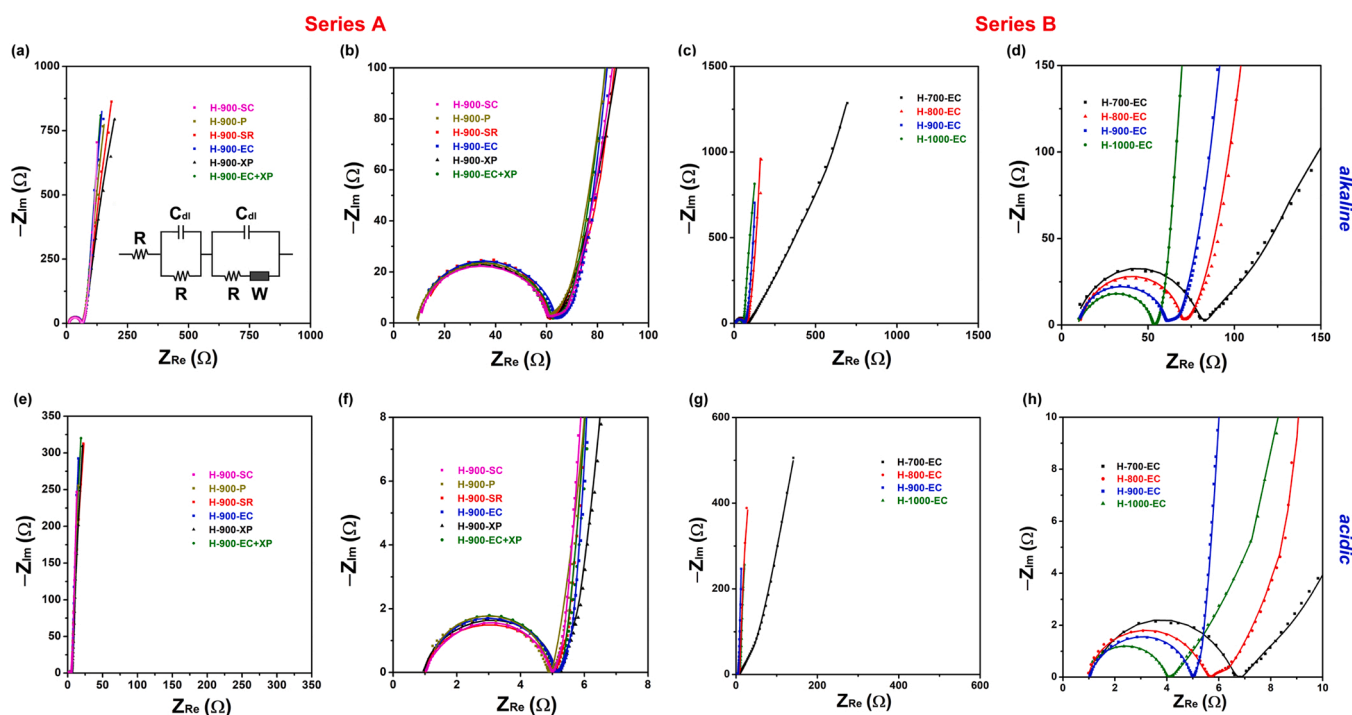


Fig. 7. Nyquist plots and fitted curves of Series A (a,e) and Series B (c,g) in terms of the equivalent circuit (inset to a), along with their high-frequency counterparts (b,f for Series A and d,h for Series B) in the alkaline (upper diagram) and acidic (lower diagram) electrolytes.

technique is used to investigate the impacts of pore width distributions. Fig. 7 shows a set of Nyquist plots for both the Series A and B electrocatalysts at low and high frequencies in aqueous KOH and H₂SO₄ solutions, alongside their respective fitted curves based on the equivalent circuit (see the inset to Fig. 7a). The parameters of charge transport (charge-transfer resistance R_{ct}) and mass transport (Warburg impedance Z_w) are readily available from the equivalent circuit [47]. The R_{ct} and Z_w values of the two series of hibiscus-based electrocatalysts in the alkaline and acidic media are summarized in Table 3. It is easy to see similarities in R_{ct} and Z_w of the same-temperature Series A electrocatalysts in either solution, signifying their similar properties in terms of charge transport and mass transport. Conversely, the same-part, different-temperature electrocatalysts exhibit the very dissimilar R_{ct} and Z_w values. The order of R_{ct} at either pH is H-700-EC > H-800-EC > H-900-EC > H-1000-EC; that is, the higher the processing temperature, the lower is the charge-transport resistance, indicating that increasing temperature helps to increase electronic conductivity. In comparison, the Z_w values that reflect mass-transport resistances fall in the order H-700-EC > H-800-EC \approx H-1000-EC > H-900-EC in both electrolytes, which correlates with the variations in their pore width distributions (Table 1). Specifically, higher porosity and lower tortuosity are more conducive to the decrease in mass-transport resistance. It is known that gas diffusion in a porous matrix is strongly dependent on porous properties, with the expression $D^{\text{eff}} = \epsilon^\tau \cdot D$ in which τ is tortuosity, ϵ is porosity, D is nominal diffusivity, and D^{eff} is effective diffusivity [48]. Clearly, τ and ϵ are associated with porous properties, whereas D , related to fluid features, can be considered as a constant when diffusing species and medium, temperature, and pressure are fixed [48]. Thus, the effective diffusivity within pores is a sensitive function of tortuosity and porosity. According to Table 1, the ϵ^τ values of H-700-EC, H-800-EC, H-900-EC, and H-1000-EC have been calculated to be 0.066, 0.15, 0.38, and 0.15, respectively, showing that D^{eff} follows the order H-900-EC > H-800-EC \approx H-1000-EC > H-700-EC, which ranks in the reverse order of their Z_w . On the basis of these data, therefore, the major impacts of pore properties as exemplified by tortuosity and porosity on mass transport have been revealed with emphasis on the processing temperature rather than the part that really matters.

Furthermore, the effects of nitrogen species distributions on electrocatalytic activities are explored using density functional theory (DFT) calculations. The Sabatier principle tells us that optimal performance can be achieved with a moderate strength of interaction between reaction intermediate and catalyst surface [49]. The absorption energies of reaction intermediates (e.g. *OOH, *O, and *OH) are linearly correlated with each other according to the scaling relationship [50], and the formation of an intermediate species *OOH is commonly regarded as the potential-determining step (PDS) of ORR taking place on nitrogen-doped carbon, so the absorption free-energy change of *OOH can be used as the

surface-related descriptor for the ORR activity [51,52]. By tuning nitrogen species distributions of catalyst surfaces, we can tailor reaction free-energy surfaces and optimize intermediate species absorption strengths, thereby leading to the decrease in activation energy and the increase in catalytic activity. Because the same-temperature Series A electrocatalysts show strong similarities in their nitrogen species distributions, their different-temperature counterparts are modelled to find out how activities are affected by variations in nitrogen. It is generally considered that pyridinic and graphitic nitrogens are the two major ORR-active nitrogen species [53–55]. Hence it is reasonable to expect that the Series B electrocatalysts can be reflected by the four models with different contents of pyridinic and graphitic nitrogens (Fig. S1). The Gibbs free-energy changes of H-700-EC, H-800-EC, H-900-EC, and H-1000-EC in terms of electrocatalytic ORR at 1.23 V are exhibited in Fig. 8a. Obviously, the PDS for H-700-EC is the generation of *OOH with an energy barrier of 1.94 eV, which is a very high energy barrier for ORR and therefore results in its poor performance. It is worth noting that as the processing temperature increases, the ratios of pyridinic to graphitic nitrogens decrease (Table 2), along with the decrease in the energy barrier for the formation of *OOH, which can be rationalized by considering the impact of nitrogen species on the electronic structure of catalyst surface. According to the literature, pyridinic nitrogen exhibits the strong sp^2 conjugate feature, whereas graphitic nitrogen does the opposite [56]. Thus, a trade-off between pyridinic and graphitic nitrogens should be able to tailor the surface absorption energy of *OOH and the resultant activity.

To confirm this, the density of state (DOS) analysis has been conducted. As shown in Fig. 8b, the gradual increase in graphitic nitrogen relative to pyridinic nitrogen because of the rise of processing temperature results in the right shift and increased magnitude of the DOSs that pass through the adjoining Fermi level, particularly for H-900-EC and H-1000-EC. The higher the DOS at the Fermi level, the stronger the tendency to donate electrons from catalyst surface to substrate species and the easier the formation of *OOH from dioxygen (which needs an electron), contributing to the lowering of the absorption energies of *OOH for H-900-EC and H-1000-EC [56,57]. In other words, a growing proportion of graphitic nitrogen owing to processing temperature increases the strength of the attractive interaction between the key intermediate *OOH and the catalyst surface. However, the excessively low ratio of pyridinic to graphitic nitrogens (occurring in H-1000-EC) makes it difficult to convert *OH to the product H₂O with an energy barrier of 0.83 eV (Fig. 8a). Only when the pyridinic/graphitic ratio is close to 1:1 (that is, H-900-EC) does the PDS energy barrier have a minimum (0.54 eV), signifying its optimum activity, as supported by the electrochemical data.

The volcano plot (Fig. 8c) shows a downward trend in the absorption free-energy change of the key intermediate *OOH for H-700-EC, H-800-

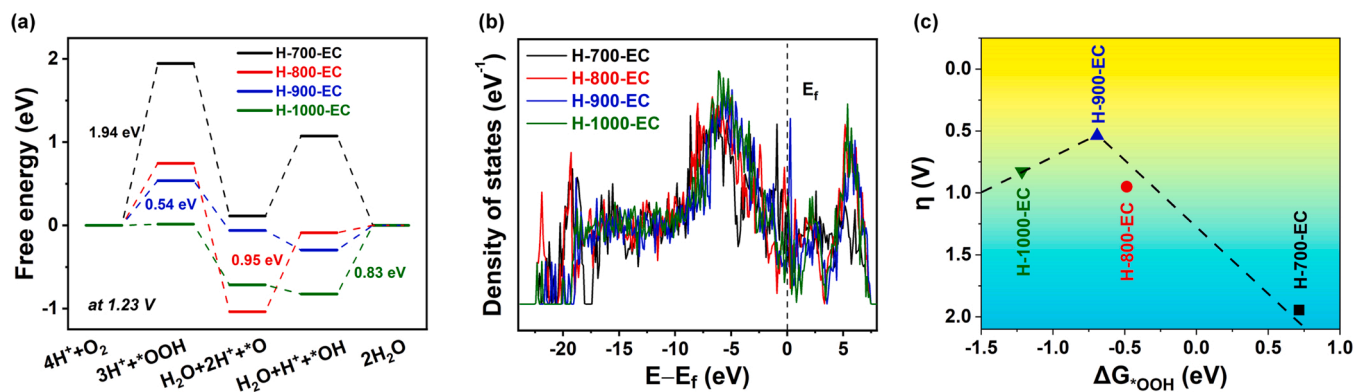


Fig. 8. Free-energy profiles of H-700-EC, H-800-EC, H-900-EC, and H-1000-EC in the electrocatalysis of O₂ reduction at 1.23 V vs. RHE (a). DOS diagram of the four models (b), with the Fermi level (E_f) being shown as a dotted line. A volcano plot of theoretical overpotential (η) at the four catalyst surfaces as a function of *OOH absorption free-energy change (c).

EC, H-900-EC, and H-1000-EC that undergo the increasing proportions of graphitic nitrogen as the processing temperature is raised. Based on the Sabatier principle, a moderate strength of interaction between *OOH and catalyst surface minimizes the energy barrier of PDS, and a case in point is H-900-EC that requires the minimum theoretical overpotential (see the vertical axis of the volcano plot). It can therefore be concluded that H-900-EC becoming the optimal electrocatalyst, from the perspective of nitrogen species distributions, is attributed to the tuning of pyridinic/graphitic ratios and the attendant absorption strength of *OOH through processing temperatures.

4. Conclusions

Centering around concerns over consistency of biomass-based electrocatalysts, we have provided the definite answer, proving that the processing temperature plays a decisive role rather than the part of biomass itself. Diverse parts of biomass, possessing different biological functions and different morphological features, all undergo convergence under thermal conditions, that is, acquiring similar structures which involve not only pore width distributions but also elemental distributions. The combination of experimental and theoretical data described above constitutes compelling evidence that the temperature-controlled distributions of pore widths and nitrogen species exert significant effects on electrocatalytic activities through the respective tailoring of mass transport and absorption strength of the key intermediate *OOH. Additionally, our results demonstrate that the variations of structures and activities of biomass-based electrocatalysts can be readily averaged out by annealing processing, making the large-scale production possible. Overall, this work informs us that dispensing with doubts as to whether biomass is reliable or not, consistent electrocatalysts prepared from biomass are readily available because type is not the determining factor.

CRediT authorship contribution statement

Wendu Zhang: Investigation, Validation, Data curation, Formal analysis, Visualization, Writing - original draft, Writing - review & editing. **Shilin Wei:** Investigation, Software, Validation, Data curation, Formal analysis, Visualization, Writing - review & editing. **Peiyao Bai:** Software, Formal analysis, Writing - review & editing. **Weiqli Liu:** Formal analysis, Writing - original draft, Writing - review & editing. **Chuangchuang Yang:** Validation, Formal analysis. **Lang Xu:** Conceptualization, Methodology, Resources, Writing - original draft, Writing - review & editing, Supervision, Project administration, Funding acquisition.

Declaration of Competing Interest

The authors declare that they have no known competing financial interests or personal relationships that could have appeared to influence the work reported in this paper.

Data Availability

Data will be made available on request.

Acknowledgements

We thank Zhongguo Xu and Xiaoli Liu for collection and classification of hibiscus. This research was supported by grants from the National Key Research and Development Program of China (2021YFB4001502), the National Natural Science Foundation of China (51702358), the Natural Science Foundation of Jiangsu Province (BK20170281), and the Fundamental Research Funds for the Central Universities (2019ZDPY02). L.X. holds the Jiangsu Specially-Appointed Professorship.

Appendix A. Supporting information

Supplementary data associated with this article can be found in the online version at doi:10.1016/j.apcatb.2023.122391.

References

- [1] S. Zhang, M. Chen, X. Zhao, J. Cai, W. Yan, J.C. Yen, S. Chen, Y. Yu, J. Zhang, Advanced noncarbon materials as catalyst supports and non-noble electrocatalysts for fuel cells and metal-air batteries, *Electrochem. Energy Rev.* 4 (2021) 336–381.
- [2] S.X.L. Luo, R.Y. Liu, S. Lee, T.M. Swager, Electrocatalytic isoxazoline-nanocarbon metal complexes, *J. Am. Chem. Soc.* 143 (2021) 10441–10453.
- [3] Y.T. Liu, L. Tang, J. Dai, J. Yu, B. Ding, Promoted electrocatalytic nitrogen fixation in Fe-Ni layered double hydroxide arrays coupled to carbon nanofibers: The role of phosphorus doping, *Angew. Chem. Int. Ed.* 59 (2020) 13623–13627.
- [4] D.S. Baek, K.A. Lee, J. Park, J.H. Kim, J. Lee, J.S. Lim, S.Y. Lee, T.J. Shin, H. Y. Jeong, J.S. Son, S.J. Kang, J.Y. Kim, S.H. Joo, Ordered mesoporous carbons with graphitic tubular frameworks by dual templating for efficient electrocatalysis and energy storage, *Angew. Chem. Int. Ed.* 60 (2021) 1441–1449.
- [5] B. Yang, J. Xu, D. Bin, J. Wang, J. Zhao, Y. Liu, B. Li, X. Fang, Y. Liu, L. Qiao, L. Liu, B. Liu, Amorphous phosphatized ruthenium-iron bimetallic nanoclusters with Pt-like activity for hydrogen evolution reaction, *Appl. Catal. B: Environ.* 283 (2021), 119583.
- [6] X. Luo, S. Chen, T. Hu, Y. Chen, F. Li, Renewable biomass-derived carbons for electrochemical capacitor applications, *SusMat* 1 (2021) 211–240.
- [7] W. Liu, S. Wei, P. Bai, C. Yang, L. Xu, Robust coal matrix intensifies electron/substrate interaction of nickel-nitrogen (Ni-N) active sites for efficient CO₂ electroreduction at industrial current density, *Appl. Catal. B: Environ.* 299 (2021), 120661.
- [8] C. Yang, P. Bai, W. Liu, S. Wei, W. Zhang, L. Xu, Optimization of pH-universal O₂ reduction electrocatalysis by precise control over structural variables via basic bathing, *Appl. Catal. B: Environ.* 303 (2022), 120912.
- [9] W. Liu, P. Bai, S. Wei, C. Yang, L. Xu, Gadolinium changes the local electron densities of nickel 3d orbitals for efficient electrocatalytic CO₂ reduction, *Angew. Chem. Int. Ed.* 61 (2022), e202201166.
- [10] S. Yuan, J. Zhang, L. Hu, J. Li, S. Li, Y. Gao, Q. Zhang, L. Gu, W. Yang, X. Feng, B. Wang, Decarboxylation-induced defects in MOF-derived single cobalt atom@carbon electrocatalysts for efficient oxygen reduction, *Angew. Chem. Int. Ed.* 60 (2021) 21685–21690.
- [11] L. Tang, Q. Xu, Y. Zhang, W. Chen, M. Wu, MOF/PCP-based electrocatalysts for the oxygen reduction reaction, *Electrochem. Energy Rev.* 5 (2022) 32–81.
- [12] S. Liu, Y. Zhang, B. Ge, F. Zheng, N. Zhang, M. Zuo, Y. Yang, Q. Chen, Constructing graphitic-nitrogen-bonded pentagons in interlayer-expanded graphene matrix toward carbon-based electrocatalysts for acidic oxygen reduction reaction, *Adv. Mater.* 33 (2021), 2103133.
- [13] M. Borghei, J. Lehtonen, L. Liu, O.J. Rojas, Advanced biomass-derived electrocatalysts for the oxygen reduction reaction, *Adv. Mater.* 30 (2018), 1703691.
- [14] Z. Zhang, S. Yang, H. Li, Y. Zan, X. Li, Y. Zhu, M. Dou, F. Wang, Sustainable carbonaceous materials derived from biomass as metal-free electrocatalysts, *Adv. Mater.* 31 (2019), 1805718.
- [15] X. Li, B.Y. Guan, S. Gao, X.W. Lou, A general dual-templating approach to biomass-derived hierarchically porous heteroatom-doped carbon materials for enhanced electrocatalytic oxygen reduction, *Energy Environ. Sci.* 12 (2019) 648–655.
- [16] L. Yu, C. Yang, W. Zhang, W. Liu, H. Wang, J. Qi, L. Xu, Solvent-free synthesis of N-doped nanoporous carbon materials as durable high-performance pH-universal ORR catalysts, *J. Colloid Interface Sci.* 575 (2020) 406–415.
- [17] L. Du, G. Zhang, X. Liu, A. Hassanpour, M. Dubois, A.C. Tavares, S. Sun, Biomass-derived nonprecious metal catalysts for oxygen reduction reaction: the demand-oriented engineering of active sites and structures, *Carbon Energy* 2 (2020) 561–581.
- [18] B.M. Matsagar, R.X. Yang, S. Dutta, Y.S. Ok, K.C.W. Wu, Recent progress in the development of biomass-derived nitrogen-doped porous carbon, *J. Mater. Chem. A* 9 (2021) 3703–3728.
- [19] W. Zhang, C. Yang, W. Liu, H. Wang, S. Wei, J. Qi, P. Bai, B. Jin, L. Xu, Long-range order, short-range disorder: Engineering one-dimensional flow channel arrays with hierarchically porous reaction interfaces for electrocatalytic reduction of oxygen, *Appl. Catal. B: Environ.* 293 (2021), 120199.
- [20] H.J. Son, Y.R. Cho, Y.E. Park, S.H. Ahn, Flexible, compressible, versatile biomass-derived freestanding carbon monoliths as binder- and substrate-free tri-functional electrodes for solid-state zinc-air batteries and overall water splitting, *Appl. Catal. B: Environ.* 304 (2022), 120977.
- [21] S. Tabac, D. Eisenberg, Pyrolyze this paper: can biomass become a source for precise carbon electrodes? *Curr. Opin. Electrochem.* 25 (2021), 100638.
- [22] Y. Zhang, S. Liu, X. Zheng, X. Wang, Y. Xu, H. Tang, F. Kang, Q.H. Yang, J. Luo, Biomass organs control the porosity of their pyrolyzed carbon, *Adv. Funct. Mater.* 27 (2017), 1604687.
- [23] S. Dutta, A. Bhaumik, K.C.W. Wu, Hierarchically porous carbon derived from polymers and biomass: effect of interconnected pores on energy applications, *Energy Environ. Sci.* 7 (2014) 3574–3592.
- [24] P. Kaur, G. Verma, S.S. Sekhon, Biomass derived hierarchical porous carbon materials as oxygen reduction reaction electrocatalysts in fuel cells, *Prog. Mater. Sci.* 102 (2019) 1–71.

- [25] S.A. Nicolae, H. Au, P. Modugno, H. Luo, A.E. Szego, M. Qiao, L. Li, W. Yin, H. J. Heeres, N. Berge, M.M. Titirici, Recent advances in hydrothermal carbonisation: from tailored carbon materials and biochemicals to applications and bioenergy, *Green. Chem.* 22 (2020) 4747–4800.
- [26] X. Tang, D. Liu, Y.J. Wang, L. Cui, A. Ignaszak, Y. Yu, J. Zhang, Research advances in biomass-derived nanostructured carbons and their composite materials for electrochemical energy technologies, *Prog. Mater. Sci.* 118 (2021), 100770.
- [27] B. Huang, Y. Liu, Z. Xie, Two dimensional nanocarbons from biomass and biological molecules: synthetic strategies and energy related applications, *J. Energy Chem.* 54 (2021) 795–814.
- [28] S.S. Sekhon, J. Lee, J.S. Park, Biomass-derived bifunctional electrocatalysts for oxygen reduction and evolution reaction: a review, *J. Energy Chem.* 65 (2022) 149–172.
- [29] G. Zhang, X. Liu, L. Wang, H. Fu, Recent advances of biomass derived carbon-based materials for efficient electrochemical energy devices, *J. Mater. Chem. A* 10 (2022) 9277–9307.
- [30] Y. Liu, J. Wang, J. Wu, Y. Zhao, H. Huang, Y. Liu, Z. Kang, Critical roles of H₂O and O₂ in H₂O₂ photoproduction over biomass derived metal-free catalyst, *Appl. Catal. B: Environ.* 319 (2022), 121944.
- [31] G. Kresse, J. Hafner, *Ab initio* molecular dynamics for liquid metals, *Phys. Rev. B* 47 (1993) 558–561.
- [32] G. Kresse, J. Hafner, *Ab initio* molecular-dynamics simulation of the liquid-metal-amorphous-semiconductor transition in germanium, *Phys. Rev. B* 49 (1994) 14251–14269.
- [33] G. Kresse, J. Furthmüller, Efficiency of *ab-initio* total energy calculations for metals and semiconductors using a plane-wave basis set, *Comput. Mater. Sci.* 6 (1996) 15–50.
- [34] G. Kresse, J. Furthmüller, Efficient iterative schemes for *ab initio* total-energy calculations using a plane-wave basis set, *Phys. Rev. B* 54 (1996) 11169–11186.
- [35] M. Thommes, K. Kaneko, A.V. Neimark, J.P. Olivier, F. Rodriguez-Reinoso, J. Rouquerol, K.S.W. Sing, Physisorption of gases, with special reference to the evaluation of surface area and pore size distribution (IUPAC Technical Report), *Pure Appl. Chem.* 87 (2015) 1051–1069.
- [36] J. Rouquerol, G. Baron, R. Denoyel, H. Giesche, J. Groen, P. Klobes, P. Levitz, A. V. Neimark, S. Rigby, R. Skudas, K. Sing, M. Thommes, K. Unger, Liquid intrusion and alternative methods for the characterization of macroporous materials (IUPAC Technical Report), *Pure Appl. Chem.* 84 (2012) 107–136.
- [37] W. Liu, J. Qi, P. Bai, W. Zhang, L. Xu, Utilizing spatial confinement effect of N atoms in micropores of coal-based metal-free material for efficiently electrochemical reduction of carbon dioxide, *Appl. Catal. B: Environ.* 272 (2020), 118974.
- [38] X. Lu, T. Li, A. Bertei, J.I.S. Cho, T.M.M. Heenan, M.F. Rabuni, K. Li, D.J.L. Brett, P. R. Shearing, The application of hierarchical structures in energy devices: New insights into the design of solid oxide fuel cells with enhanced mass transport, *Energy Environ. Sci.* 11 (2018) 2390–2403.
- [39] O.H. Kim, Y.H. Cho, S.H. Kang, H.Y. Park, M. Kim, J.W. Lim, D.Y. Chung, M.J. Lee, H. Choe, Y.E. Sung, Ordered macroporous platinum electrode and enhanced mass transfer in fuel cells using inverse opal structure, *Nat. Commun.* 4 (2013) 2473.
- [40] C.V. Nguyen, S. Lee, Y.G. Chung, W.H. Chiang, K.C.W. Wu, Synergistic effect of metal-organic framework-derived boron and nitrogen heteroatom-doped three-dimensional porous carbons for precious-metal-free catalytic reduction of nitroarenes, *Appl. Catal. B: Environ.* 257 (2019), 117888.
- [41] L. Wang, K. Liang, L. Deng, Y.N. Liu, Protein hydrogel networks: a unique approach to heteroatom self-doped hierarchically porous carbon structures as an efficient ORR electrocatalyst in both basic and acidic conditions, *Appl. Catal. B: Environ.* 246 (2019) 89–99.
- [42] W. Zhang, J. Qi, P. Bai, H. Wang, L. Xu, High-level nitrogen-doped, micro/mesoporous carbon as an efficient metal-free electrocatalyst for the oxygen reduction reaction: optimizing the reaction surface area by a solvent-free mechanochemical method, *N. J. Chem.* 43 (2019) 10878–10886.
- [43] S. Ma, J. Deng, Y. Xu, W. Tao, X. Wang, Z. Lin, Q. Zhang, L. Gu, W. Zhong, Pollen-like self-supported FeIr alloy for improved hydrogen evolution reaction in acid electrolyte, *J. Energy Chem.* 66 (2022) 560–565.
- [44] T. Wu, Z. Xu, X. Wang, M. Luo, Y. Xia, X. Zhang, J. Li, J. Liu, J. Wang, H.L. Wang, F. Huang, Surface-confined self-reconstruction to sulfate-terminated ultrathin layers on NiMo₃S₄ toward biomass molecule electro-oxidation, *Appl. Catal. B: Environ.* 323 (2023), 122126.
- [45] S. Drespe, F. Luo, R. Schmack, S. Kühn, M. Gliech, P. Strasser, An efficient bifunctional two-component catalyst for oxygen reduction and oxygen evolution in reversible fuel cells, electrolyzers and rechargeable air electrodes, *Energy Environ. Sci.* 9 (2016) 2020–2024.
- [46] Z. Li, R. Ma, Q. Ju, Q. Liu, L. Liu, Y. Zhu, M. Yang, J. Wang, Spin engineering of single-site metal catalysts, *Innovation* 3 (2022), 100268.
- [47] A.J. Bard, L.R. Faulkner, *Electrochemical Methods: Fundamentals and Applications*, second ed., Wiley, New York, 2001.
- [48] R. O'Hayre, S.W. Cha, W.G. Colella, F.B. Prinz, *Fuel Cell Fundamentals*, third ed., Wiley, Hoboken, 2016.
- [49] T. Bligaard, J.K. Nørskov, S. Dahl, J. Matthiesen, C.H. Christensen, J. Sehested, The Brønsted-Evans-Polanyi relation and the volcano curve in heterogeneous catalysis, *J. Catal.* 224 (2004) 206–217.
- [50] A. Kulkarni, S. Siahrostami, A. Patel, J.K. Nørskov, Understanding catalytic activity trends in the oxygen reduction reaction, *Chem. Rev.* 118 (2018) 2302–2312.
- [51] H. Jiang, J. Gu, X. Zheng, M. Liu, X. Qiu, L. Wang, W. Li, Z. Chen, X. Ji, J. Li, Defect-rich and ultrathin N doped carbon nanosheets as advanced trifunctional metal-free electrocatalysts for the ORR, OER and HER, *Energy Environ. Sci.* 12 (2019) 322–333.
- [52] M.T.M. Koper, Analysis of electrocatalytic reaction schemes: distinction between rate-determining and potential-determining steps, *J. Solid State Electrochem* 17 (2013) 339–344.
- [53] Y.N. Sun, J. Yang, X. Ding, W. Ji, A. Jaworski, N. Hedin, B.H. Han, Synergetic contribution of nitrogen and fluorine species in porous carbons as metal-free and bifunctional oxygen electrocatalysts for zinc-air batteries, *Appl. Catal. B: Environ.* 297 (2021), 120448.
- [54] J.A. Behan, E. Mates-Torres, S.N. Stamatin, C. Domínguez, A. Iannaci, K. Fleischer, M.K. Hoque, T.S. Perova, M. García-Melchor, P.E. Colavita, Untangling cooperative effects of pyridinic and graphitic nitrogen sites at metal-free N-doped carbon electrocatalysts for the oxygen reduction reaction, *Small* 15 (2019), 1902081.
- [55] X. Ning, Y. Li, J. Ming, Q. Wang, H. Wang, Y. Cao, F. Peng, Y. Yang, H. Yu, Electronic synergism of pyridinic- and graphitic-nitrogen on N-doped carbons for the oxygen reduction reaction, *Chem. Sci.* 10 (2019) 1589–1596.
- [56] P. Bai, W. Liu, C. Yang, S. Wei, L. Xu, Boosting electrochemical performance of activated carbon by tuning effective pores and synergistic effects of active species, *J. Colloid Interface Sci.* 587 (2021) 290–301.
- [57] T. Schiros, D. Nordlund, L. Pálková, D. Prezzi, L. Zhao, K.S. Kim, U. Wurstbauer, C. Gutiérrez, D. Delongchamp, C. Jaye, D. Fischer, H. Ogasawara, L.G. M. Pettersson, D.R. Reichman, P. Kim, M.S. Hybertsen, A.N. Pasupathy, Connecting dopant bond type with electronic structure in N-doped graphene, *Nano Lett.* 12 (2012) 4025–4031.